THE JOURNAL OF PHYSICAL CHEMISTRY B

ARTICLE

pubs.acs.org/JPCB

Coaxial Electrospun Poly(methyl methacrylate)−Polyacrylonitrile Nanofibers: Atomic Force Microscopy and Compositional Characterization

Nicole E. Zander,*[†,‡] Kenneth E. Strawhecker,[†] Joshua A. Orlicki,[†] Adam M. Rawlett,[†] and Thomas P. Beebe, Jr.[‡]

[†]U.S. Army Research Laboratory, Weapons and Materials Research Directorate, Aberdeen Proving Ground, Maryland 21005, United States

[‡]Department of Chemistry and Biochemistry, University of Delaware, Newark Delaware 19716, United States

S Supporting Information

ABSTRACT: Poly(methyl methacrylate) (PMMA)−polyacrylonitrile (PAN) fibers were prepared using a conventional single-nozzle electrospinning technique. The as-spun fibers exhibited core−shell morphology as verified by transmission electron microscopy (TEM) and atomic force microscopy (AFM). AFM-phase and modulus mapping images of the fiber cross-section and X-ray photoelectron spectroscopy (XPS) analysis indicated that PAN formed the shell and PMMA formed the core material. XPS, thermogravimetric analysis (TGA), and elemental analysis were used to determine fiber compositional information. Soaking the fibers in solvent demonstrated removal of the core material, generating hollow PAN fibers.

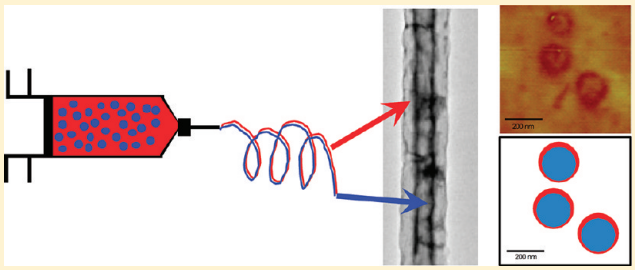

INTRODUCTION

Bicomponent core−sheath electrospun fibers offer many advantages over traditional single material fibers, including the ability to control and tailor the mechanical and electrical properties, as well as the ability to form hollow fibers by postspinning removal of the core material. In addition, nonelectrospinnable materials such as low molecular weight or conjugated polymers with limited solubility can be fabricated into fibers by formation in the core phase with an electrospinnable sheath material, followed by removal of the shell.[1−5] Nanoparticles or biomolecules can be encapsulated in the core material with their release controlled by the sheath material properties, which gives rise to core−sheath fiber applications in the drug-delivery field.[6−9] In addition, a synthetic polymer can be used as a structural core support for a biocompatible sheath polymer to improve scaffold mechanical properties for tissue engineering applications.[10,11]

Core−shell fibers are traditionally made by either electrospinning the core material, which serves as a template for the deposition of the shell material by chemical vapor, plasma, or solution deposition, or by the use of a coannular nozzle.[12−14] The former technique has the drawback of requiring two steps to form the bicomponent fibers and the attendant issues associated with sheath-diameter uniformity. The latter technique requires a careful balance of viscosity and miscibility of the two polymer solutions to ensure continuous entrainment of the core material within the shell material, as well as sufficiently low interfacial tension between the core and shell solutions.[10] Recently, researchers have reported the formation of core−shell fibers using a single nozzle technique that eliminates many of the drawbacks associated with the two-stage or coannular nozzle methods.[15,16] In the aforementioned work, emulsion solutions of polyacrylonitrile (PAN) and poly(methyl methacrylate) (PMMA) were prepared in dimethylformamide (DMF). Phase separation between the polymers occurred in which the lower surface tension PAN formed the continuous outer phase and PMMA droplets remained dispersed in the surrounding PAN/DMF matrix. With proper choice of electrospinning conditions, the electrostatic forces acting on the PAN outer phase stretched the PMMA droplets to form a continuous inner phase, resulting in the fabrication of core−shell fibers.

PAN electrospun fibers are an attractive material because they can readily be pyrolyzed/carbonized to form carbon nanofibers. Carbon nanofibers have many applications in adsorbents, polymer reinforcement, catalyst supports for fuel cells, as well as energy storage devices due to their high surface area, mechanical strength, and electrical conductivity.[17,18] Core−shell fibers with PAN as the shell material allow for the formation of hollow carbon nanofibers after removal of the core material and pyrolysis/carbonization. Hollow or porous carbon materials are known to have enhanced properties in catalysis, sensors, and electronic and separation devices.[19−24]

Although it is known that core−shell nanofibers can be fabricated using a single-nozzle from PMMA−PAN solutions, to the best of our knowledge, the chemical composition of the

Received: June 14, 2011
Revised: August 15, 2011
Published: September 19, 2011

ACS Publications © 2011 American Chemical Society

core and shell layers has not been characterized or quantified, nor has the precise locations of the two polymers in the bicomponent fiber been mapped. In addition, the mechanical properties of the two layers have not been characterized on the local (i.e., single-fiber) scale. In this work, we have used the surface-sensitive technique of X-ray photoelectron spectroscopy (XPS), along with the bulk-sensitive thermogravimetric analysis (TGA) technique to calculate the composition of the two polymers in the bicomponent fibers. In addition, we have used a novel atomic force microscope (AFM) technique to map the elastic modulus of each polymer.

MATERIALS

PAN (M_w = 150 kDa), PMMA (M_w = 540 kDa), and anhydrous DMF were obtained from Sigma-Aldrich and used as received. RTESP and HMX AFM tips, as well as the HarmoniX PS-LDPE reference sample were obtained from Veeco. Epo-thin resin and hardener were obtained from Fisher.

METHODS

Fabrication of Electrospun Fibers. A 12 wt % emulsion/solution consisting of a mixture of 6 wt % each of PAN in DMF and PMMA in DMF was stirred overnight at room temperature (RT). The concentration of the PAN and PMMA solutions used to form control fibers was chosen based on the viscosity measured with a viscometer (Brookfield Cap 2000). For controls, a 12 wt % solution of PAN and a 10 wt % solution of PMMA were prepared in DMF. PMMA−PAN fibers were electrospun using a custom built apparatus consisting of a syringe pump (Aladdin AL-1000) and a rotating 6-in.-wide, 1-in.-diameter mandrel. The mandrel was connected to a motor (Dayton 115 V AC) with a speed controller, allowing the mandrel to rotate at speeds between 0 and 8000 rpm. A 5 mL syringe was filled with polymer solution and fed through an 18-gauge stainless steel needle at a flow rate of 1 mL/h with an applied potential of 15 kV. The gap between the needle and the collecting mandrel was fixed at 7 in., and the collecting mandrel was held at an applied potential of −3 kV. Electrospun fibers were dried under vacuum at RT overnight before characterization.

Characterization of Electrospun Fibers. The morphology of the fiber scaffolds was examined using a field-emission scanning electron microscope (SEM; Hitachi S-4700) in the secondary-electron mode, using a mixture of upper and lower detectors. An accelerating voltage of 0.6 kV was maintained in order to prevent surface damage to the fibers. Before observation, the fibers were coated with approximately 10 nm of gold using a sputter coater (Hummer XP Sputtering System, Anatech LTD). Several areas were imaged in order to examine the uniformity of the fiber diameters. Fiber diameters were measured using image analysis software (Image-J, National Institutes of Health).

Transmission electron microscopy (TEM) was used to collect real space images of each sample. Imaging was performed on a JEM-2100F field emission TEM (JEOL USA, Inc.) operated at 200 kV. Bright-field images were collected using an 11 megapixel SC1000 Orius CCD camera (Gatan, Inc.). Image analysis was performed using Digital Micrograph (Gatan, Inc.).

Surface compositional analysis was performed using a Kratos Axis Ultra 165 XPS system equipped with a hemispherical analyzer. Sampling areas of 1 mm × 0.5 mm were irradiated with a 100 W monochromatic Al Kα (1486.7 eV) beam and takeoff angles of 10° and 90°. The XPS chamber pressure was maintained between 10^{-9} and 10^{-10} Torr. Elemental high resolution scans were collected with a 20-eV pass energy for the C 1s, O 1s, and N 1s core levels. A value of 284.6 eV for the methylene component of the C 1s spectrum was used as the calibration energy for the binding energy scale, and all other spectra were shifted by the corresponding amount. Data were processed using Casa XPS software.

Near-surface chemical analysis was performed by Fourier transform infrared spectroscopy−attenuated total reflectance (FTIR-ATR) (Thermo Nicolet Nexus 870 ESP) using 256 averaged scans and 4 cm^{-1} resolution over a range of 4000−400 cm^{-1}. FTIR-ATR spectra were collected using a Specac IR sampling accessory with a germanium crystal in multibounce mode.

The bulk chemical composition was characterized on a TA Instrument Thermogravimetric Analyzer (TGA Q 5000) under nitrogen flow. All samples were heated at 10 °C/min to 1000 °C. The TGA data were processed using Universal Analysis software.

AFM was used to determine the elastic modulus and AFM-phase differences between the PAN and PMMA regions of the coaxial fibers. Images were obtained using a Dimension 3100 AFM with a Nanoscope V-controller in modulus mapping mode. Commercial AFM tips (RTESP and HMX from Veeco) were used as received. Intermittent-contact mode (i.e., tapping mode) images were obtained using the standard mode-1 resonant frequency of the RTESP probes, nominally 311−355 kHz, with an amplitude set point of approximately 80% of the free-air oscillation amplitude, and an x-scan rate of 0.5−1.0 Hz. Elastic modulus was determined using the Veeco HarmoniX software. The HMX probes were calibrated using a standard sample composed of a copolymer of polystyrene and low-density polyethylene (PS−LDPE), following the calibration method outlined previously.[25] A minimum of 10 spots were averaged in each image to determine the local modulus by binning together 16 to 36 pixels (4 × 4 to 6 × 6 pixels) due to noise in the image. To compare the measured modulus values from the AFM-modulus mapping to the corresponding noise levels, regions from the same images were evaluated using region averaging (roughness analysis command) as well as section analysis (both in the standard Veeco analysis software, V7.30r1Sr3). The cross-analysis with AFM-phase images of the self-same regions further confirmed the apparent morphology obtained from this technique. To prepare the samples for such analysis, cross sections of the fibers were prepared. Fiber mats were cut, placed between steel clips, set in epoxy, and cured at RT overnight. Samples were then polished according to standard polymer processing protocols until the sample surfaces were optically flat.

Compositional Analysis. The composition of the bicomponent fibers was estimated by XPS using a simplex optimization module in the CASA software. Briefly, the background was subtracted for the spectra of the PMMA−PAN fibers as well as for PAN and PMMA single component fibers, and the intensity scale was set to unity for all samples. The peak components of the bicomponent fiber sample were fit with the PAN and PMMA component peaks using a Simplex minimization fitting algorithm.[26] Experimental composition was determined using TGA by dividing the weight percent remaining after pyrolysis of the PMMA−PAN bicomponent fiber samples by that of the PAN fiber control. This assumes that all mass from the PMMA component in the bicomponent fiber leaves the samples as a gas after pyrolysis. Composition was determined with AFM by

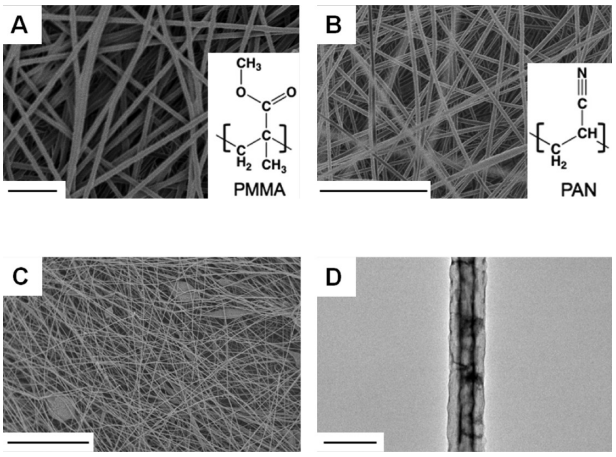

Figure 1. SEM and TEM micrographs of electrospun fibers. (A) PMMA fibers, having a diameter of 480 ± 40 nm (n = 50, scale bar =5 μm); (B) PAN fibers, having a diameter of 180 ± 35 nm (n = 50, scale bar = 5 μm); (C) PMMA−PAN fibers formed from an emulsion/solution consisting of a 50/50 mixture of each polymer at 6 wt % in DMF, having a diameter of 75 ± 25 nm (n = 50, scale bar = 5 μm); (D) TEM of a single PMMA−PAN fiber formed from an emulsion solution consisting of a 50/50 mixture of each polymer at 6 wt % in DMF (scale bar = 200 nm). Note core−shell morphology observed in panel D. This particular fiber, prepared separately from those shown in panel C, exhibited a core diameter of ∼50 nm, a sheath wall thickness of ∼40 nm, and an overall diameter of ∼130 nm.

measuring estimated fiber diameters in AFM-phase and modulus images, calculating geometrical volume fractions assuming coaxial cylinders, and determining the fractional composition using polymer densities and molecular weights.

Statistics. All data are expressed as mean ± standard deviation (SD) unless noted. One-way ANOVA with *post hoc* Tukey means comparison tests and unpaired Student's t-tests were conducted with a significance level of $p < 0.05$.

RESULTS

Core−sheath fibers composed of PAN and PMMA were electrospun using a single nozzle technique. PAN and PMMA single-component fibers were also prepared as controls. The concentrations of the control solutions were chosen to match the viscosity of the PMMA−PAN emulsion solution. SEM images of the fibers are displayed in Figure 1A−C. The fiber diameters spun from the emulsion (Figure 1C) were the smallest at 75 ± 25 nm (n = 50), whereas the PAN fibers (Figure 1B) were larger at 180 ± 35 nm (n = 50), and the PMMA fibers (Figure 1A) were significantly larger at 480 ± 40 nm (n = 50). TEM was utilized to examine the interior structure of the PMMA−PAN fibers (Figure 1D). A core−shell morphology is clearly visible. This particular fiber consisted of a core having a diameter of c.a. 65 nm, surrounded by a sheath having a wall thickness of c.a. 48 nm. Cross-sectional SEM imaging was also attempted, but sufficient resolution was not achieved due to the small fiber diameters of the emulsion samples.

The cross-sectional morphology of the fibers was also examined using AFM and axially oriented fibers embedded in an epoxy matrix. AFM-phase images were collected in intermittent-contact mode and are shown in Figure 2. Cross sections of the fibers were visible in all phase images, but only the PMMA−PAN fiber cross sections (Figure 2C) exhibited the biphase or core−shell

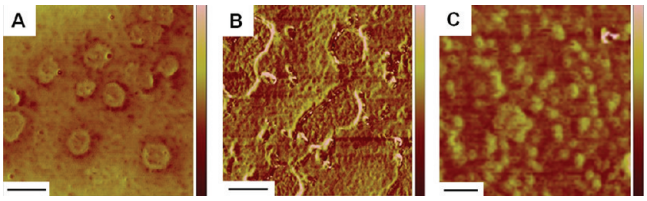

Figure 2. AFM phase images of electrospun fiber cross sections. (A) PAN fibers, (scale bar = 0.5 μm); (B) PMMA fibers (scale bar = 1 μm); (C) PMMA−PAN fibers (scale bar = 0.2 μm). This overview image, covering 1.7 μm × 1.7 μm, shows the relatively close packing density of the PMMA−PAN core−shell fibers fabricated from an emulsion/solution. A high-resolution image and analysis of individual core−shell fibers is presented in Figure 3.

morphology, as evidenced by the donut-like features in most of the fibers (seen more clearly in Figure 3). Some of the fibers displayed evidence of some shell material within the core. This was not unexpected due to the single nozzle fiber formation process, which potentially allowed mixing of the two phases, as well as some demixing that could have occurred just prior to electrospinning. The polishing process may have also introduced modifications to the intrinsic as-spun structure.

The Young's modulus was determined using the relatively new AFM-modulus mapping variation of scanning probe microscopy, as shown in Figure 3. Representative AFM-phase (Figure 3A) and modulus (Figure 3B) images along with a corresponding section analysis line scan of the modulus image (Figure 3C) and image histogram (Figure 3D) are shown for the PMMA−PAN coaxial fibers. Note that the embedding matrix consisted of a traditional hard epoxy bedding material. The AFM-phase image (Figure 3A) shows that the fiber had softer core domains (dark phase contrast), suggesting that the core is composed primarily of PMMA. The AFM-modulus map of the area in the dotted rectangle of Figure 3A is seen in Figure 3B. It shows clear distinction in the modulus between the two fibers and their surrounding epoxy, but a core−shell fiber morphology was not observed in the AFM-modulus images.

A cursor profile through the fiber in the upper-right corner of Figure 3B is seen in Figure 3C, and the corresponding histogram of all pixel values in Figure 3B is shown in Figure 3D. It can be seen in both the histogram and line profiles that the center of the fiber exhibited an apparent local modulus of 0.34 ± 0.16 GPa. The surroundings of the fibers, consisting presumably of the bedding epoxy, exhibited an apparent local modulus of 0.96 ± 0.21 GPa.

The measurement of apparent feature dimensions in the (x,y) sample plane is not a straightforward process because the tip shape is convoluted with the object's feature size in scanning probe techniques. However, assuming that the core and sheath structures are approximately in the same plane as a result of the sample polishing procedure, and since the phase and modulus image maps were simultaneously collected with the same tip, it was nevertheless informative to compare the apparent feature sizes as determined by AFM-phase and modulus maps. The apparent fiber diameters measured in the AFM-phase channel were found to be approximately 50% larger than the diameters of the same fibers in the modulus channel.

Table 1 displays the average modulus of the PAN, PMMA, and PMMA−PAN fibers, as well as the modulus of PAN and PMMA films observed by the same methods. The modulus differences between the PAN and epoxy were not found to be statistically

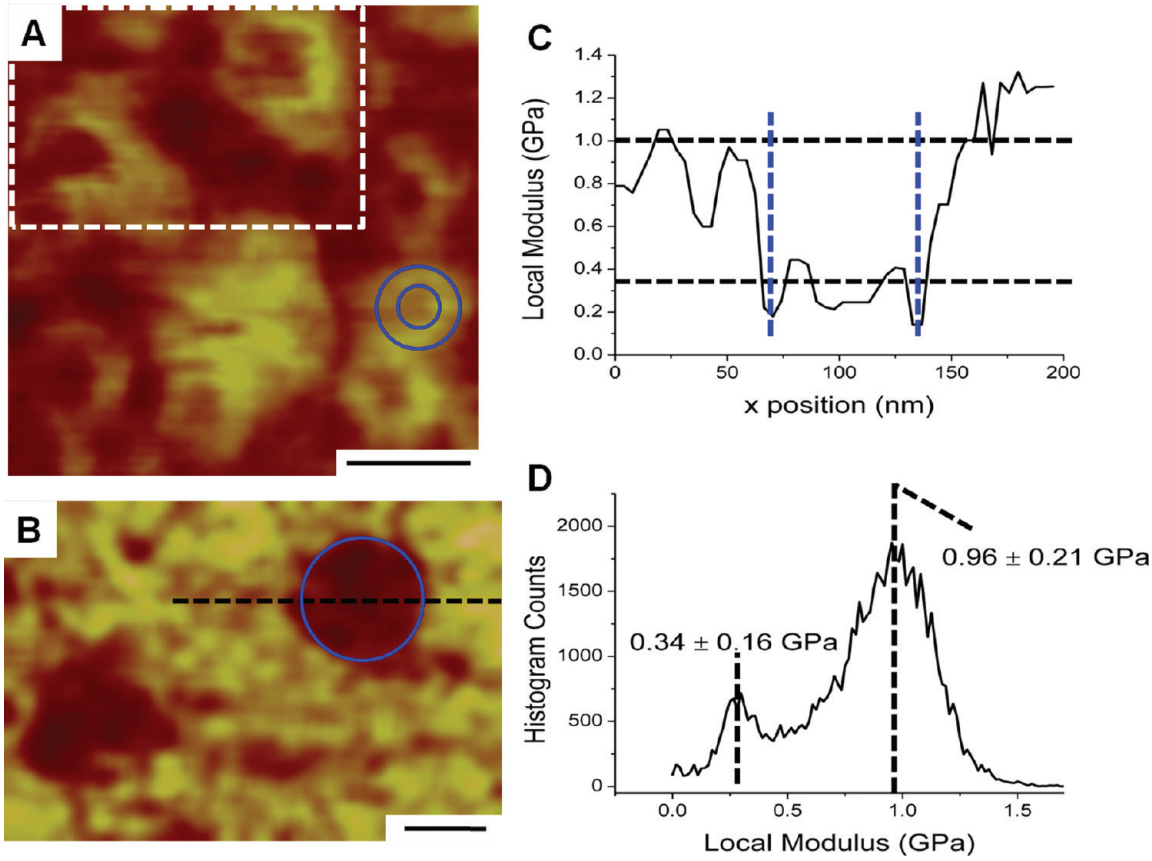

Figure 3. Detailed analysis of images obtained by AFM-phase and AFM-modulus modes on cross sections of electrospun core−sheath fibers. (A) AFM-phase image showing roughly nine core−sheath fibers of the same approximate size (one fiber is indicated by concentric blue circles with inner circle diameter ∼35 nm and outer circle diameter ∼70 nm). The dashed rectangle indicates the area in which AFM-modulus data were obtained for subsequent parts of this figure (scale bar = 100 nm). (B) AFM-modulus image of the upper-left corner of panel A, showing two fibers, although not exhibiting enough contrast/resolution to resolve the fiber's core from the fiber's sheath (scale bar = 50 nm). The diameter of the overlaid circle is 75 nm. (C) Cursor profile drawn at the position indicated in panel B. The position of the overlaid 75-nm circle is indicated as vertical blue lines for reference. The horizontal black dashed lines are drawn at modulus values that correspond to the centroids in the histogram of panel D. (D) Pixel intensity histogram of the entire area of panel B, showing a bimodal distribution of moduli values having centroids of 0.34 ± 0.16 GPa and 0.96 ± 0.21 GPa.

Table 1. Young's Modulus of Electrospun PAN and PMMA Fiber and Films As Determined by AFM Modulus Imaging[a]

sample	polymer	local elastic modulus (GPa)
PMMA-PAN core-shell fiber	epoxy	0.93 ± 0.12
	PMMA	0.31 ± 0.03 *
	PAN	0.88 ± 0.15 *
PMMA fiber	epoxy	0.94 ± 0.10
	PMMA	0.33 ± 0.04 *
PAN fiber	epoxy	0.82 ± 0.20
	PAN	0.76 ± 0.15
PMMA (bulk control film)	PMMA	0.75 ± 0.19
PAN (bulk control film)	PAN	1.57 ± 0.27 *

[a] Error bars represent mean ± SD (*significantly different, $p < 0.05$).

significant, which provides an explanation for the apparent smaller fiber diameters observed in the modulus channel as the fiber shell was not discernible. The Young's modulus values for both the PMMA (330 ± 40 MPa) and PAN (760 ± 150 MPa) phases compared reasonably well to literature values of electrospun fibers from single-fiber tensile tests (73 ± 30 MPa for PMMA, 800 ± 400 MPa for PAN).[27,28] The AFM-measured moduli for the control bulk films were higher than those found by AFM for the fibers (0.75 ± 0.19 GPa for PMMA films; 1.57 ± 0.27 GPa for PAN films) most likely due to the size effect.[29] In all cases, PAN had a Young's modulus approximately twice that of PMMA.

The determination of the local modulus at each point in the fiber cross-section allowed for the mapping of the locations of the two polymer phases within the bicomponent PMMA−PAN fibers. This information coupled with chemical analysis techniques enabled the determination of the chemical makeup of the core and shell materials. The AFM-phase images complemented by the modulus data show that the stiffer/higher modulus PAN formed the outer shell of the fibers, whereas the lower modulus PMMA comprised the inner material.

Near-surface chemical composition of the PMMA−PAN fibers was probed transverse to the fiber axis with FTIR-ATR, as seen in Figure 4. In Figure 4B, a strong peak at 2040 cm^{-1} for the nitrile stretch present in PAN can be seen in the PAN fibers as well as in the PMMA−PAN fibers. In Figure 4 A, a set of peaks around 1485 cm^{-1} denote the O═C−O normal mode present in PMMA. Spectra IV in Figure 4A,B display the spectrum of

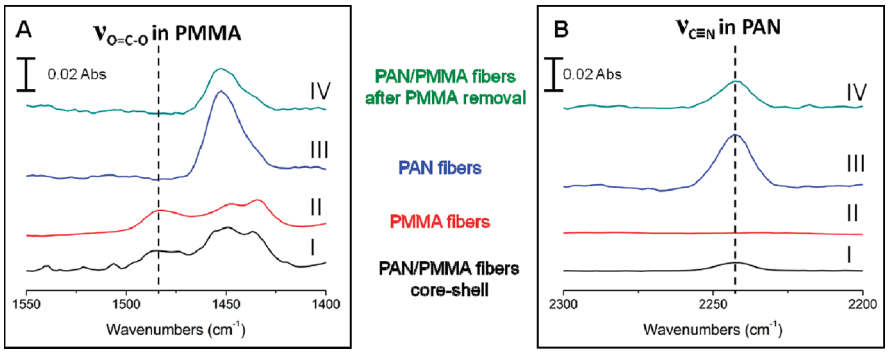

Figure 4. FTIR-ATR spectra of electrospun fibers. (A) O═C−O mode in PMMA: (I) PMMA−PAN core−shell fibers, (II) PMMA fibers, (III) PAN fibers, (IV) PMMA−PAN core−shell fibers soaked in chloroform to remove PMMA. (B) nitrile stretch in PAN: (I) PAN/PMMA core−shell fibers, (II) PMMA fibers, (III) PAN fibers, (IV) PMMA−PAN core−shell fibers soaked in chloroform to remove PMMA. Dashed lines denote positions of peaks of interest.

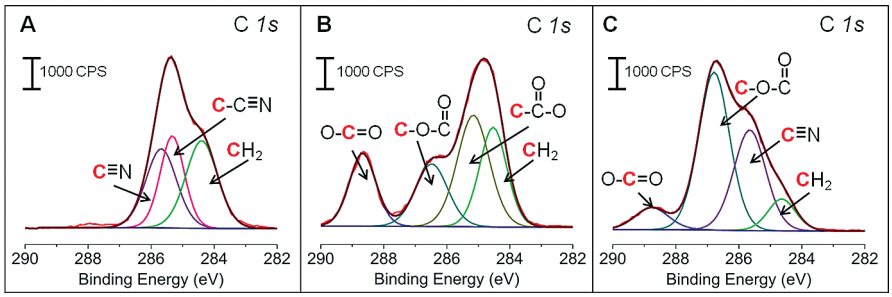

D

sample	C	O	N	N/C
PMMA (nominal bulk)	71.4	28.6	-	-
PAN (nominal bulk)	75.0	-	25.0	0.33
PMMA fibers (n = 6)	73.0 ± 0.6	26.9 ± 0.6	-	-
PAN fibers (n = 6)	78.0 ± 0.3	3.0 ± 0.9	19.0 ± 0.8	0.23 ± 0.04
PMMA-PAN fibers (n = 6)	77.5 ± 0.4	5.5 ± 0.5	17.0 ± 0.3	0.22 ± 0.02*
Soaked PMMA-PAN fibers (n = 6)	78.1 ± 0.5	2.4 ± 0.3	19.5 ± 0.2	0.25 ± 0.01*
PMMA-PAN fibers 10° TOA (n = 6)	77.2 ± 0.4	5.6 ± 0.2	17.3 ± 0.6	0.23 ± 0.04

Figure 5. High-resolution C 1s X-ray photoelectron spectra of electrospun fibers. (A) PAN fibers; (B) PMMA fibers; (C) PMMA−PAN core−shell fibers. (D) Atomic composition of electrospun fibers as determined by XPS. All samples were collected at a 90° takeoff angle, except as noted in the last line of the table. Error bars represent mean ± SD (*significantly different, $p < 0.05$).

PMMA−PAN fibers after they were soaked in chloroform to remove the PMMA phase (PAN is not soluble in chloroform). The soaked fiber spectrum was nearly identical to that of the PAN-only fibers (III), indicating removal of the PMMA phase. The shell (approximately 48 nm wall thickness) surrounding the core of the fibers is most likely not a perfect, impenetrable cladding, able to prevent the infiltration of a solvent. Thus, we infer that the removal of PMMA occurs by solvent action.

The surface chemistry of the fibers was also examined transverse to the fiber axis using XPS, which probes the top 1−10 nm of the fiber surface dependent on the takeoff angle. The high-resolution C 1s spectra are displayed in Figure 5A−C. XPS spectra of the PAN fibers (Figure 5A) were well fitted with three main carbon components in nearly equivalent ratios, consisting of the methylene or hydrocarbon (37.3%), the carbon bonded to the nitrile group (29.9%), and the carbon of the nitrile group (32.8%). XPS spectra of the PMMA fibers (Figure 5B) were well fitted with four main carbon components, consisting of the methylene or hydrocarbon (26.6%), the carbon bonded to the carbonyl (34.9%), the carbon bonded to the oxygen of the ester (19.6%), and the carbon of the ester (18.8%). XPS spectra of the PMMA−PAN bicomponent fibers were well fitted with four main carbon components, consisting of a blend between the major PAN and PMMA components, as seen in Figure 5C. The components consisted of the methylene or hydrocarbon component (9.1%), the nitrile carbon (33.2%), the carbon bonded to the oxygen of the ester (50.1%), and the carbon of the ester (7.6%). The atomic compositions and the nitrogen-to-carbon ratios are displayed in Figure 5D. The nitrogen-to-carbon ratio was highest for the chloroform-soaked bicomponent fibers

Table 2. Molar and Weight Composition of Electrospun PMMA-PAN Fibers as Determined by XPS, TGA, AFM, and Elemental Analysis[a,b]

method or sample	mole %		weight %	
	PAN	PMMA	PAN	PMMA
XPS 90° takeoff angle ($n = 6$)	78.5 ± 1.7	21.5 ± 1.7	50.3 ± 4.1	49.6 ± 4.1
XPS 10° takeoff angle ($n = 2$)	84.9 ± 2.1	15.1 ± 2.1	61.0 ± 3.9	39.0 ± 3.9
XPS 90° takeoff angle (soaked sample) ($n = 6$)	87.0 ± 0.04	13.0 ± 0.04	65.0 ± 0.07	35.0 ± 0.07
TGA (typical error 0.4%)	91.6	8.4	75.1	24.9
AFM (based on estimated fiber diameters) ($n = 6$)	86.3 ± 1.7	13.6 ± 1.7	63.6 ± 4.1	36.3 ± 4.1
elemental analysis (typical error 0.3%)	86.5	13.5	64.0	36.0

[a] As spun from an emulsion of 50/50 (by weight) PAN/PMMA in DMF. [b] XPS samples were collected at either a 10° or 90° takeoff angle as noted in the table.

(0.25 ± 0.01), and was similar to that of the PAN fibers (0.23 ± 0.04). The chloroform-soaked bicomponent fibers were shown with FTIR-ATR to be composed primarily of PAN. As expected, the nitrogen-to-carbon ratio was slightly reduced for the bicomponent fibers due to the presence of the oxygen-containing groups in the PMMA. When the XPS takeoff angle was reduced to 10°, or near the grazing angle, the nitrogen-to-carbon ratio of the bicomponent fibers (0.23 ± 0.04) was similar to that of single-component PAN fibers (0.23 ± 0.04). Since smaller takeoff angles correspond to a more surface-sensitive measurement (i.e., smaller sampling depths), PAN-related XPS signals were expected since PAN was shown to be present in the outer layer of the coaxial fibers based on the AFM imaging experiments discussed above.

TGA was used to determine the bulk composition of the PAN and PMMA polymers in the core−shell fibers. The TGA plot of neat PAN fibers revealed weight loss events at 300 and 450 °C. The TGA plot for PMMA contained only a single weight loss event at 430 °C. The plot of the bicomponent fibers had weight loss events at 300 and 420 °C. The derivative weights were calculated, and neat PAN fibers were found to have 46.1 wt % remaining after carbonization in nitrogen, whereas the PMMA fibers completely decomposed, leaving no mass. The PMMA−PAN fibers had 35.7 wt % remaining, which suggested that the fibers were composed of up to 75.1 wt % PAN and 24.9 wt % PMMA.

Composition information for the PMMA−PAN bicomponent fibers is summarized for various analytical methods (XPS, TGA, AFM, and elemental analysis) in Table 2 for fiber mats produced by spinning from a 50/50 (by weight) emulsion of PMMA−PAN. XPS analysis of the fiber surface obtained at the 90° takeoff angle using a Simplex algorithm as discussed above showed the experimental PAN composition to be 78.5 ± 1.7 mol percent. The XPS-determined PAN composition was higher at a 10° takeoff angle, as expected, and similar to the soaked bicomponent fiber sample, the AFM-determined composition, and elemental data, when compared to 90° XPS takeoff angle, since the surface was enriched in the PAN polymer. TGA analysis revealed the bulk molar composition of PAN to be higher than the compositions determined by both XPS and AFM. These trends are summarized in Table 2.

■ DISCUSSION

One possible explanation for the high PAN concentration calculated by TGA is that the char layer formed by PAN reduced the flammability of PMMA.[30] Thus, the weight percent remaining for the bicomponent fiber sample could have contributions from both polymer phases, and the TGA calculation assumed that all PMMA was pyrolyzed. Another explanation observed by previous researchers was that solvent in the emulsion solution preferentially diluted the PAN phase.[15] In the aforementioned work, the researchers found that PAN was diluted such that the actual concentration of PAN in the solution was significantly lower than expected, although the concentration of PAN in the fibers was not determined in their work. To test this theory, an experiment in which viscosity measurements were recorded for the emulsion solution over time was performed. The solution separated into two phases and the viscosity of the less-dense PAN phase decreased to less than 30% of its original value in 3 h, while the viscosity of the more-dense PMMA phase increased more than 3-fold over this same time period.

Possibly, the reduced viscosity of the PAN phase allowed for better fiber formation during the electrospinning process, whereas the more concentrated PMMA solution may have primarily remained in the stretched or rod-like droplet, or was largely left behind in the syringe, thereby incorporating less PMMA into the spun fibers. Dilution of the PAN phase could also explain the reason the fiber diameters were smaller for the core−shell fibers when compared to neat PAN fibers formed from a solution of similar viscosity.

Bazilevsky et al. postulated a mechanism based on the trapping of PMMA droplets at the base of the Taylor cone, just prior to expansion, whereby the electrostatic forces act at the outer surface to stretch the trapped PMMA droplet into a geometry that eventually becomes surrounded by PAN upon expansion.[15] Kim et al. found that surface tension played an important role in controlling the cross-sectional morphology.[16] The lower surface tension PAN polymer occupied the continuous phase of the solution while the higher surface tension PMMA polymer formed the discontinuous phase. The researchers found that the core PMMA phase formed a discontinuous rod-like phase in the fiber interior. In our work, modulus mapping with AFM also provided evidence of a continuous PAN phase in the fiber shell and a PMMA core.

It was found here that the modulus of PAN and the epoxy were not statistically different. Thus, while the AFM-phase images showed core−shell morphology, only the core region was visible in the modulus images. The dynamic range of the image contrast in the AFM-modulus images was low, and the signal-to-noise ratio was only slightly greater than 2. Thus the fiber diameters appeared to be approximately 50% smaller in the AFM-modulus image when compared to the AFM-phase image. Thus, the choice of matrix is of great importance in terms of modulus so that the fibers embedded within it can be easily distinguished.

Nonetheless, the AFM-modulus imaging provided complementary information to the AFM-phase images, allowing the location of the two polymer phases in the AFM-phase image to be determined based on their modulus.

CONCLUSIONS

Core−shell electrospun fibers composed of PAN and PMMA were prepared from an emulsion using a single-nozzle technique that relied on phase separation to generate the coaxial morphology. TEM and AFM imaging provided evidence of this core−shell morphology, and a novel AFM technique that measures the local Young's modulus provided a means to map the location of each polymer phase. For the bicomponent fiber samples prepared in this work, the PAN polymer was found to comprise the shell material and the PMMA polymer the core. FTIR and XPS analysis of the chemical composition of the samples provided evidence of both polymers present in the bicomponent fiber samples. After soaking the core−shell fibers in chloroform, a good solvent for PMMA but not for PAN, removal of the PMMA core was observed, thus forming hollow PAN fibers. In the future, such hollow PAN fibers could be pyrolyzed to form hollow carbon nanofibers. In addition, angle-resolved XPS of bicomponent fiber samples showed that the PAN composition increased relative to PMMA for small takeoff angles, indicating that PAN formed the shell material and PMMA formed the core material. XPS, elemental analysis, and TGA experiments were also utilized to determine the molar composition of the two polymers in the as-spun core−shell fibers. All techniques confirmed a higher concentration of PAN in the fibers than expected, which may have been due to preferential dilution of the PAN phase by the solvent, the lower surface tension of the PAN solution compared to that of PMMA, or the formation of a char layer during TGA analysis.

ASSOCIATED CONTENT

Supporting Information. TEM images of PMMA−PAN fibers formed from an emulsion solution consisting of a 50/50 mixture of each polymer at 6 wt % in DMF are displayed in (A)−(C). Scale bar is 100 nm. Note the core−shell morphology observed. This material is available free of charge via the Internet at http://pubs.acs.org.

AUTHOR INFORMATION

Corresponding Author

*E-mail: nicole.e.zander.civ@mail.mil. Tel: 410 306-1965. Fax: 410 306-0676.

ACKNOWLEDGMENT

This work was conducted at both the University of Delaware in Newark, DE, and the U.S. Army Research Laboratory in Aberdeen Proving Ground, MD. This work was supported by matching funds associated with the University of Delaware's Center of Biomedical Research Excellence entitled *Molecular Design of Advanced Biomaterials*, an NIH COBRE Center (2P20-RR017716), and by the U.S. Army.

REFERENCES

(1) Cao, G; Brinker, C. J. *Annual Review of Nano Research*; World Scientific: Hackensack, NJ, 2006.
(2) Sun, Z.; Zussman, E.; Yarin, A. L.; Wendorff, J. H.; Greiner, A. *Adv. Mater.* **2003**, *15*, 1929–1932.
(3) Yu, J. H.; Fridrikh, S. V.; Rutledge, G. C. *Adv. Mater.* **2004**, *16*, 1562–1566.
(4) Li, D.; Babel, A.; Jenekhe, S. A.; Xia, Y. *Adv. Mater.* **2004**, *16*, 2062–2066.
(5) Greiner, A.; Wendorff, J. H.; Yarin, A. L.; Zussman, E. *Appl. Microbiol. Biotechnol.* **2006**, *71*, 387393.
(6) Huang, Z. M.; Zhang, Y.; Ramakrishna, S. *J. Polym. Sci. B: Polym. Phys.* **2005**, *43*, 2852–2861.
(7) Jiang, H.; Hu, Y.; Li, Y.; Zhao, P.; Zhu, K.; Chen, W. *J. Controlled Release* **2005**, *108*, 237–243.
(8) Sun, B.; Duan, B.; Yuan, X. *J. Appl. Polym. Sci.* **2006**, *102*, 39–45.
(9) Srikar, R.; Yarin, A. L.; Megaridis, C. M.; Bazilevsky, A. V.; Kelley, E. *Langmuir* **2008**, *24*, 965–974.
(10) Moghe, A. K.; Gupta, B. S. *Polym. Rev.* **2008**, *48*, 353–377.
(11) Zhang, Y. Z.; Venugopal, J.; Huang, Z. M.; Lim, C. T.; Ramakrishna, S. *Biomacromolecules* **2005**, *6*, 2583–2589.
(12) Zussman, E.; Yarin, A. L.; Bazilevsky, A. V.; Avrahami, R.; Feldman, M. *Adv. Mater.* **2006**, *18*, 348–353.
(13) Li, D.; Xia, Y. *Nano Lett.* **2004**, *4*, 933–938.
(14) Loscertales, I. G.; Barrero, A.; Marquez, M.; Spretz, R.; Velarde-Ortiz, R.; Larsen, G. *J. Am. Chem. Soc.* **2004**, *126*, 5376–5377.
(15) Bazilevsky, A. V.; Yarin, A. L.; Megaridis, C. M. *Langmuir* **2007**, *23*, 2311–2314.
(16) Kim, C.; Jeong, Y. I.; Ngoc, B. T. N.; Yang, K. S.; Kojima, M.; Kim, Y. A.; Endo, M.; Lee, J. *Small* **2007**, *3*, 91–95.
(17) Nataraj, S. K.; Kim, B. H.; Yun, J. H.; Lee, D. H.; Aminabhavi, T. M.; Yang, K. S. *Mater. Sci. Eng., B* **2008**, *162*, 75–81.
(18) Zhou, Z.; Lai, C.; Zhang, L.; Qian, Y.; Hou, H.; Reneker, D. H.; Fong, H. *Polymer* **2009**, *50*, 2999–3006.
(19) Kaneko, K.; Imai, J. *Carbon* **1989**, *27*, 954–955.
(20) Joo, S. H.; Choi, S. J.; Oh, I. W.; Kwak, J. Y.; Liu, Z.; Terasaki, O.; Ryoo, R. *Nature* **2001**, *412*, 169–172.
(21) Schlapbach, L.; Zuttel, A. *Nature* **2001**, *414*, 353–358.
(22) Terrones, M. *Annu. Rev. Mater. Res.* **2003**, *33*, 419–501.
(23) Bekyarova, E.; Murata, V.; Yudasaka, M.; Kasuya, D.; Iijima, S.; Tanaka, H.; Kaneko, K. J. *Phys. Chem. B* **2003**, *107*, 4681–4684.
(24) Take, H.; Matsumoto, T.; Yoshino, K. *Synth. Met.* **2003**, *135*, 731–732.
(25) Sahin, O. *Rev. Sci. Instrum.* **2007**, *78*, 103707–103711.
(26) Fairley, N.; Carrick, A. *The Casa Cookbook*; Acolyte Science: Cheshire, U.K., 2005.
(27) Liu, L.; Tasis, D.; Prato, M.; Wagner, H. D. *Adv. Mater.* **2007**, *19*, 1228–1233.
(28) Qin, X. *J. Therm. Anal. Calorim.* **2010**, *99*, 571–575.
(29) Li, X.; Ono, T.; Wang, Y.; Esashi, M. *Appl. Phys. Lett.* **2003**, *83*, 3081–3083.
(30) Gilman, J. W.; Jackson, C. L.; Morgan, A. B.; Harris, R. *Chem. Mater.* **2000**, *12*, 1866–1873.